THE JOURNAL OF PHYSICAL CHEMISTRY C
A JOURNAL OF THE AMERICAN CHEMICAL SOCIETY

pubs.acs.org/JPCC

Article

Kerogen Swelling in Light Hydrocarbon Gases and Liquids and Validity of Schroeder's Paradox

Zheng Li, Jun Yao, and Abbas Firoozabadi*

Cite This: *J. Phys. Chem. C* 2021, 125, 8137–8147

Read Online

ACCESS | Metrics & More | Article Recommendations | Supporting Information

ABSTRACT: Kerogen is often the organic part of the shale and provides the pore space for a large part of the hydrocarbons in place. Kerogen molecules are flexible like polymer molecules, and may swell when in contact with specific solvents. The difference in swelling of a polymer when exposed to a pure liquid versus its saturated vapor is known as Schroeder's paradox, which has a long history of controversy. To the best of our knowledge, kerogen swelling induced by a hydrocarbon in both gas and liquid states has not been investigated. We investigate the sorption of gaseous and liquid propane, normal butane, and normal pentane in kerogen and kerogen swelling at various pressures. A flexible kerogen matrix is created using molecular dynamics simulations. The large pores are created and maintained with a dummy particle and nailed atoms, respectively. The hydrocarbon sorption and kerogen swelling induced by the sorption of hydrocarbon gases and liquids are investigated by the hybrid molecular dynamics-grand canonical Monte Carlo simulations. Results show that smaller hydrocarbon molecules in both gas and liquid states have higher sorption and induce higher swelling and structural changes in the kerogen matrix. Hydrocarbon liquids have higher sorption and induce higher kerogen swelling than the corresponding gases at saturation pressure in agreement with Schroeder's paradox. Hydrocarbon gases lead to the moderate kerogen swelling from expansion of large pores; hydrocarbon liquids swell the kerogen more significantly not only by expanding the large pore but also by creating new pores and throats. Liquid-inducing kerogen swelling is accompanied by hydrocarbon dissolution in the kerogen matrix altering significantly the pore surface area, porosity, and pore size distribution. The work sets the stage for further studies considering the effect of production on shale volumetric strain.

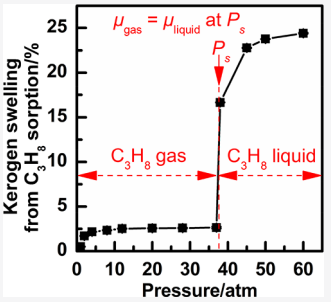

1. INTRODUCTION

The world energy production landscape has experienced a remarkable change in recent years. Development of shale formations in the United States (U.S.) has turned the country from a net energy importer to a net energy exporter in 2019.[1] Since 2018, the U.S. has eclipsed Saudi Arabia and Russia to become the world's largest oil producer.[2] The U.S. is expected to become the second largest oil exporter by 2024.[3] The enormous progress toward energy independence in the U.S. has inspired many other countries including China with large energy demands and abundant shale resources to accelerate production of natural gas and light oil from shales.[4] Shale gas and shale light oil have the advantage over coal of being clean-burning. Shale formations are complex compared to the inorganic formations in which conventional oil and gas reside. The recovery of hydrocarbon fluids from shale formations is much lower than that in conventional formations.[4] There is a need to develop shale formations more efficiently. Basic knowledge and understanding of physics of rock–fluid interactions[5,6] and subsurface volumetric strains from production will facilitate improvement in a broad range of topics from the production rate to recovery efficiency.

A large portion of hydrocarbon fluids in shale formations reside in organic nanopores. Most of the organic matters in shale rocks are made of kerogen molecules. Hydrocarbon fluids in the kerogen matrix can be classified into three different states: adsorbed states on the pore surfaces, free molecules similar to a bulk phase states in larger pores, and dissolved state in the kerogen matrix.[7−10] Hydrocarbons are believed to be produced mainly from the free molecules and to a lesser degree from the adsorbed and the dissolved molecules.[11−13] In this paper, both hydrocarbon adsorption and hydrocarbon dissolution in the kerogen matrix are collectively referred to as hydrocarbon sorption. Sorption will induce kerogen swelling,[14−16] which will then change the porosity and permeability and affect subsurface flow and production.[17]

There have been extensive experiments on the adsorption of gases in shales and kerogens.[18−23] However, experiments on gas sorption-induced shale swelling are limited.[24,25] The extensive experiments performed on liquid sorption-induced kerogen swelling[26−32] have mainly been conducted at room conditions. Larsen et al.[33−36] have measured swelling of different types of kerogen; the measured swelling is in the range of 10 to 25% in normal pentane (n-C_5H_{12}) and normal

Received: November 17, 2020
Revised: March 27, 2021
Published: April 13, 2021

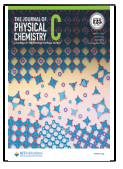

https://doi.org/10.1021/acs.jpcc.0c10362
J. Phys. Chem. C 2021, 125, 8137–8147

heptane (n-C_7H_{16}). Kelemen et al.[37] report that Type II kerogen can swell 23 and 21% in normal decane (n-$C_{10}H_{22}$) and normal hexadecane (n-$C_{16}H_{34}$), respectively. In another publication, Kelemen et al.[38] have measured the swelling of Type II kerogens (from 20 to 44%) and Type III-C kerogens (from 8 to 26%) in n-$C_{10}H_{22}$ and n-$C_{16}H_{34}$ at temperatures as high as 150 °C. The data show weak effects of temperature but strong effects of kerogen maturity and solvent type on kerogen swelling. Savest et al.[39,40] report the swelling of an Estonian shale sample and the extracted kerogen to be 5% and 10%, respectively, in normal hexane (n-C_6H_{14}). They find that the thermal pretreatment of a sample may affect swelling.[40] Recently Liang et al.[41] have conducted swelling measurements in different hydrocarbon liquids in a kerogen sample. The results show that in normal alkanes swelling decreases as the chain length increases. The alkanes include hydrocarbons from n-C_5H_{12} to normal tetradecane (n-$C_{14}H_{30}$).

Molecular simulations have been used in recent years to investigate kerogen swelling in gases and liquids. The main methods are grand canonical Monte Carlo (GCMC) simulations,[42−44] molecular dynamics simulations (MD)[45,46] and the hybrid MD-GCMC simulations.[14,16] In the GCMC simulations, one can compute an adsorption isotherm by allowing adsorbates to adsorb in the pre-constructed kerogen matrix at a specified temperature and chemical potential (μ, which can be specified through pressure and fugacity coefficient). The kerogen frame is fixed during adsorption in the GCMC simulations. Then, the adsorption-induced volumetric strain is calculated by the extended poromechanical model[47,48] in which the adsorption amount, the bulk modulus of kerogen, and coupling coefficients of adsorbates are predefined. The adsorption amount is from the GCMC simulations, and the other two parameters are measured experimentally. Swelling can be calculated directly based on a deformable kerogen matrix in MD simulations. In one investigation, the hydrocarbon molecules and the kerogen molecules are initially mixed at a fixed ratio. Then, the annealing process is conducted in an isothermal−isobaric (NPT) ensemble where the system volume is free to change. At equilibrium the swelling can be calculated through the volumes of the mixed kerogen−fluid system and the pure kerogen system. This approach may not represent the adsorption process, and the swelling may depend on the mixing ratio. In the hybrid MD-GCMC approach, the kerogen matrix is constructed first through the annealing process based on the MD simulations. Then, the kerogen matrix alternatively undergoes GCMC simulations and MD simulations until reaching equilibration. The dynamics of sorption and the sorption-induced swelling are simulated by GCMC and MD, respectively. The hybrid MD-GCMC method is a powerful method and does not require predefined parameters. It takes the advantage of both GCMC and MD simulations. The above methods have been used to study kerogen swelling in light hydrocarbon gases and carbon dioxide (CO_2). Simulation results of swelling in gases show that CO_2 makes kerogen swell the most,[14,42,44] followed by methane (CH_4), ethane (C_2H_6), and propane (C_3H_8) in the order of molecular size.[16] Additionally, the temperature,[43,45] pressure,[45] kerogen maturities,[44] and preloaded water contents[44] affect kerogen swelling in gases. There have been very limited studies on kerogen swelling in hydrocarbon liquids by molecular simulations. Pathak et al.[45] calculated a swelling of around 20% for Type II kerogen in n-C_7H_{16}, n-$C_{10}H_{22}$, and octane (C_8H_{18}) by MD simulations. Based on the hybrid MD-GCMC method, Tesson and Firoozabadi[16] report a 9% swelling of Type II-A kerogen in liquid n-C_5H_{12}. Liu et al.[49,50] have calculated CO_2 sorption in kerogen and kerogen swelling in n-C_5H_{12} and n-C_7H_{16} liquids based on the perturbed chain-statistical associating fluid theory (PC-SAFT). The results for the immature, partially mature, and mature kerogen show agreement with experimental swelling data (that is, in the range of 10 to 25%).[33,36]

Different bias schemes have been proposed to increase the insertion acceptance rate in GCMC simulations of complex adsorbate molecules.[51−54] The configurational-bias GCMC (CB-GCMC) method based on the Rosenbluth sampling scheme[55] has been widely applied to simulate adsorption of long-chain hydrocarbons in metal−organic frameworks (MOFs),[56−65] zeolite,[66−70] and confined slits.[71−73] Instead of inserting the molecule as a whole, CB-GCMC starts with one atom of the chain and inserts the molecule part by part biasing the growth process toward energetically favorable configurations in the void space of porous materials.[74] The process is effective in reducing the overlap between adsorbents and adsorbates and accelerating the convergence. The CB-GCMC simulations are conducted in the grand canonical ensemble with an invariant volume.

In summary, hydrocarbon gas-induced kerogen swelling has been mainly investigated by simulations; hydrocarbon liquid-induced kerogen swelling has been mainly studied through experiments. To the best of our knowledge, kerogen swelling by hydrocarbons in gas and liquid states close to saturation pressure has not been investigated. There may be similarities in swelling of kerogen and other flexible molecules like polymers. Many authors have claimed that polymer swelling induced in liquid and gas states at saturation pressure should be the same. This is based on the equality of chemical potentials.[75,76] In the framework of classic phase equilibrium thermodynamics in polymeric networks, the swelling is solely linked to the solvent chemical potential regardless of solvent phase states.[75,76] More than a century ago, Schroeder reported a 25-time higher polymer swelling in liquid water than in water vapor at saturation pressure. The difference in swelling at saturation pressure is known as Schroeder's paradox.[77] Schroeder's paradox has been confirmed in various experiments by different authors.[78−83] A number of authors have questioned the validity of the data and have related the difference to experimental artifacts.[84,85] In the last several years, there has been renewed interest in Schroeder's paradox in the polymer membrane fuel cells where water in contact with the membrane may be either in a liquid or gas state.[86] Water uptake and membrane swelling influence the membrane conductivity, which affect the fuel cell performance.[82,87−89] The same topic in relation to sorption and swelling in gases and liquids is very relevant in hydrocarbon extraction from shale formations. The sorption and extraction of hydrocarbons in different phase states in kerogen matrix may determine kerogen deformations. The deformation will change the porosity and permeability of the matrix and influence the subsurface flow.[14,15,17,90] The main motivation of this work is investigation of hydrocarbon sorption, kerogen swelling, and validity of Schroeder's paradox in the kerogen−hydrocarbon system.

This work centers on the use of the hybrid MD-GCMC simulations to investigate kerogen swelling induced by the sorption of gas and liquid propane (C_3H_8), normal butane (n-C_4H_{10}), and normal pentane (n-C_5H_{12}).

https://doi.org/10.1021/acs.jpcc.0c10362
J. Phys. Chem. C 2021, 125, 8137−8147

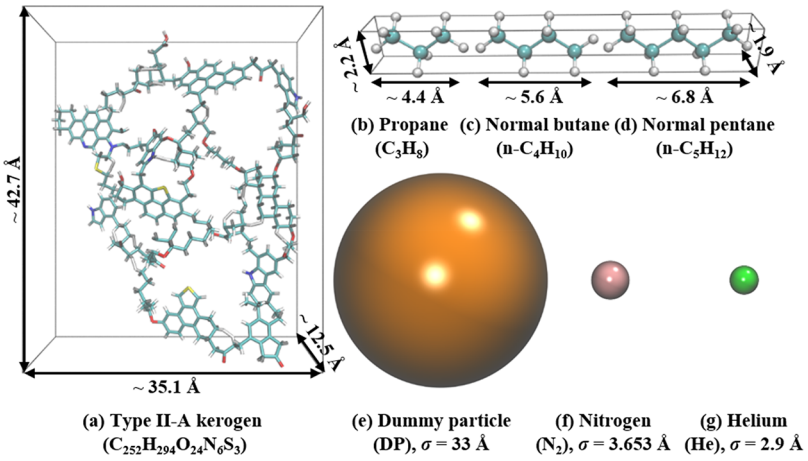

Figure 1. Atomistic models of (a) Type II-A kerogen ($C_{252}H_{294}O_{24}N_6S_3$), (b) propane ($C_3H_8$), (c) normal butane ($n$-$C_4H_{10}$), (d) normal pentane ($n$-$C_5H_{12}$), (e) dummy particle (DP), and probe particles: (f) nitrogen (N_2) and (g) helium (He). Color code: C (cyan), H (white), O (red), N (blue), S (yellow), DP (orange), N_2 (pink), and He (green).

2. MODELS AND METHODS

2.1. Molecular Models. Ungerer et al.[91] have developed a suite of kerogen molecules. Among the proposed molecules, Type II (i.e., II-A, II-B, II-C, and II-D) kerogens are representatives of oil-prone organic matter deposited in marine anoxic environments, covering type from conventional to unconventional and the maturity levels from immature to overmature.[91,92] This work adopts the immature Type II-A kerogen model ($C_{252}H_{294}O_{24}N_6S_3$), which is depicted in Figure 1a. Hydrocarbon molecules in this paper include C_3H_8, n-C_4H_{10}, and n-C_5H_{12} (Figure 1b–d). The phase state can change from the gas state to liquid state with increasing pressure under a specified temperature. Our adsorbate molecules are larger than the CH_4 and CO_2 molecules used in many recent simulations. A dummy particle (DP) shown in Figure 1e is used to create large pores in the kerogen matrix in the construction process. Without DP, the pores will be too small to accommodate large hydrocarbon molecules. Details of the construction will be presented in Section 2.2. The diameter (σ) of DP is 33 Å. The energy parameter (ε) and mass of DP are set as 0.023 kcal/mol and 1.0 g/mol, respectively. The probe particles including nitrogen (N_2) and helium (He) are selected to determine the porosity and the pore surface area of the created kerogen matrix (Section 2.4). The N_2 molecule is simplified as a single particle and the sizes of N_2 and He particles are 3.653 and 2.9 Å, respectively (Figure 1f,g).

2.2. Kerogen Matrix Construction. MD simulations are applied to construct the kerogen matrix using the large-scale atomic/molecular massively parallel simulator (LAMMPS)[93] with all-atom polymer consistent force field plus (PCFF+ force field).[94] Ungerer et al.[94,95] have verified the accuracy of the PCFF+ force field to reproduce the kerogen thermodynamic properties. The MedeA software[96] is used to assign the atom types and charges as well as other force field parameters for kerogen atoms. The cut-off distance for both Lenard–Jones (LJ) and Coulombic interactions is 9.5 Å. For long-range LJ interactions, tail corrections are applied to the energy and pressure. Long-range Coulombic interactions are computed by the particle–particle particle–mesh (PPPM) method[97,98] with an accuracy of 1×10^{-5}. Non-bonded interactions between atoms directly connected with one bond and separated by two or three bonds are excluded. The Waldman–Hagler combining rule[99] is used for LJ coefficients (i.e., σ and ε) for interactions between unlike species. Periodic boundary conditions are applied to all three directions.

The construction of the kerogen matrix follows the methodology in our recent work.[16] Initially, seventeen Type II-A kerogen molecules and one DP are randomly placed in the cubic simulation box with a side length of 150 Å as shown in Figure 2a. Then, the kerogen box undergoes a complete relaxation through successive simulations in canonical (NVT)

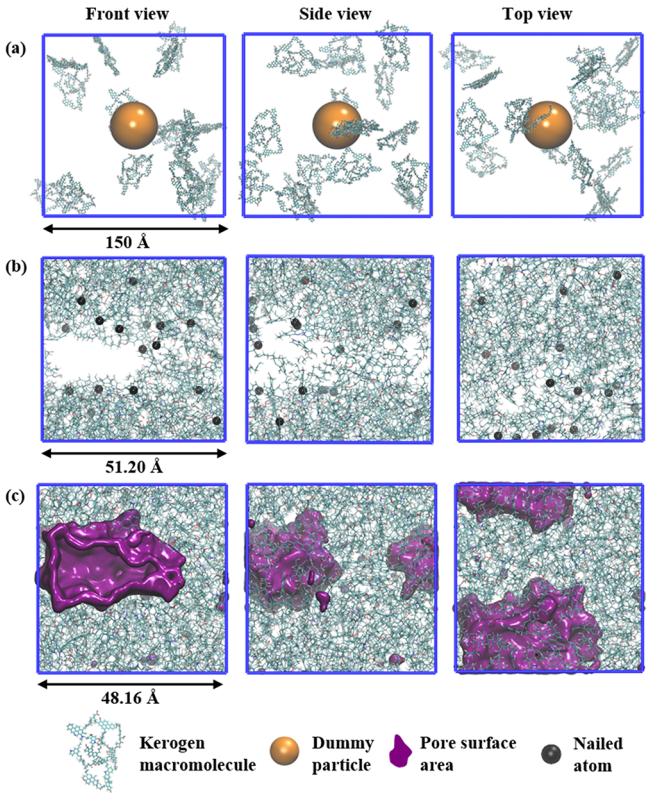

Figure 2. Front, side, and top views of the simulation box at different stages of the molecular dynamics relaxation procedure. (a) Initial simulation box with one dummy particle. (b) Simulation box of stage 9 without a dummy particle but with 17 nailed atoms marked in black. (c) Pore surface area of the kerogen matrix at the end of stage 9: T = 363.15 K and P = 1 atm.

https://doi.org/10.1021/acs.jpcc.0c10362
J. Phys. Chem. C 2021, 125, 8137–8147

and isothermal−isobaric (NPT) ensembles. The temperature and the pressure are controlled by the Nosé−Hoover thermostat[100,101] with a damping factor of 100 fs and the Nosé−Hoover barostat[102,103] with a damping factor of 1000 fs, respectively. The relaxation procedure and the corresponding timestep are summarized in Table 1. First, NVT simulation at a relatively low temperature (363.15 K) is performed in the kerogen box to reach an equilibrium state with lower energy. Then, the kerogen box is heated to a high temperature (1000 K) followed by a 1 ns simulation in the NVT ensemble. Next, the temperature is decreased from 1000 K to 363.15 K through a series of stepwise cooling simulations in the NPT ensemble at 100 atm. By further decreasing the pressure from 100 to 1 atm, the system achieves the target temperature and pressure conditions of 363.15 K and 1 atm, respectively. Finally, another 10 ns NPT simulations are performed at the target condition before removing the DP. The simulations are long enough at each stage in the annealing process (stage 1 to stage 8) to reach equilibrium (temperature and pressure changes can be seen in Figure S1).

Table 1. Molecular Dynamics Relaxation Procedure to Create the Flexible Kerogen Matrix

stage	ensemble	T/K	P/atm	time/ns	step/fs	notes
1	NVT	363.15		1	1	with DP
2	NVT	363.15 → 1000		1	0.1	
3	NVT	1000		1	1	
4	NPT	1000 → 700	100	1	0.1	
5	NPT	700 → 500	100	1	0.1	
6	NPT	500 → 363.15	100	1	0.1	
7	NPT	363.15	100 → 1	1	0.1	
8	NPT	363.15	1	10	1	
9	NPT	363.15	1	100	1	without DP but with nailed atoms

DP removal leaves a kerogen matrix with large and connected pores (Figure 2b). Without DP, another 100-ns NPT simulation is conducted and the final configuration is shown in Figure S2. Pores in the kerogen matrix collapse as described in ref 16. To prevent the large pores from collapsing from confining pressure, Tesson and Firoozabadi[16] nailed several atoms at the periphery of the pores. Specifically, the nailed atoms are located at the centers of different polyaromatic clusters in kerogen molecules. These nailed atoms are excluded from the time integration to keep them stationary so that they act as ball joints and the polyaromatic clusters act as barriers to prevent the shrinkage of the pore. Based on our recent work,[16] we chose 17 nailed atoms, which are highlighted in small black spheres in Figure 2b. In Figure S3, one of the polyaromatic clusters is magnified to show the position of the nailed atom. A detailed discussion on f nailing of selected atoms is presented in the Supporting Information. After removal of the DP with nailed atoms, a 100 ns NPT simulation is conducted at the target condition (stage 9); the final configuration is shown in Figure 2c. The structural characteristics of the final kerogen matrix in Figure 2c and Figure S2 are presented in Table 2. The nailing of atoms prevents the collapse of large pores and can provide a kerogen matrix with a porosity of about 13%. The porosity is larger than 10% because the temperature (363.15 K) is higher than that in ref 16, which is 298.15 K.

Table 2. Structural Characteristics of the Kerogen Matrix without DP after 100 ns NPT Relaxation (T = 363.15 K, P = 1 atm) without (Figure S2) and with (Figure 2c) 17 Nailed Atoms

	structural characteristics				
system	box side length (Å)	bulk density (g/cm^3)	skeletal density (g/cm^3)	porosity (%)	accessible area (m^2/g)
without DP and without nailed atoms (Figure S2)	46.25	1.11	1.13	2.01	49.48
without DP and with nailed atoms (Figure 2c)	48.16	0.98	1.13	13.04	381.90

2.3. Kerogen Matrix Deformation. Kerogen matrix deformation induced by hydrocarbon sorption is investigated by the hybrid MD-GCMC simulations using LAMMPS.[93] The PCFF+ force field is applied to hydrocarbon molecules by MedeA software.[96] The force field has been widely used to describe the interactions between kerogen and hydrocarbons.[16,90,94,95,104] MD simulations are carried out in the NPT ensembles with a timestep of 0.1 fs. Other MD parameters are set to be the same as those in Section 2.2. In the hybrid MD-GCMC simulations, 1000 GCMC steps are first conducted followed by 10,000 MD steps; then, one GCMC step is performed after every 10,000 MD steps until equilibration. Each GCMC step includes 2500 GCMC exchanges (deletions and insertions with equal probability) and 2500 Monte Carlo (MC) moves (translations and rotations with equal probability). In the GCMC simulations, the chemical potential (μ) is constant and specified by pressure and the corresponding fugacity coefficient.[16] The fugacity coefficient is calculated by the Thermosolver software.[105,106] The temperature and pressure conditions in the NPT simulations are the same as those specified in GCMC simulations. In this way, the kerogen matrix deforms under a zero effective stress condition in the NPT ensembles where the deformation is maximum.[14] All the simulations are conducted at a temperature of 363.15 K. The number of hydrocarbon molecules in the GCMC steps will fluctuate; the total number of molecules should be updated before the MD step. In each hybrid MD-GCMC simulation, the temperature, pressure, volume, and loading are monitored to determine that the equilibrium is reached. Different systems need different periods to equilibrate. In our work, simulations last 10 ns to reach equilibrium and we allow 3 ns for data collection. Figure S4 shows the evolution of box side length and loading in the simulation period.

2.4. Characterization Methods. The methods used to determine swelling (Q_v), porosity (Φ), pore surface area (S_a), and pore size distribution (PSD) of the kerogen matrix are presented in this section.

To calculate Q_v, the volume of the kerogen matrix in Figure 2c is taken as the reference volume (V_r). The swelling is given by $Q_v = (V_a - V_r)/V_r \times 100\%$, where V_a is the equilibrium volume of kerogen matrix after hydrocarbon sorption.

Calculations of Φ, S_a, and PSD follow the MC routines outlined by Gelb and Gubbins.[107,108] N_2 and He particles are used to calculate S_a and Φ, respectively. Φ is calculated by

https://doi.org/10.1021/acs.jpcc.0c10362
J. Phys. Chem. C 2021, 125, 8137−8147

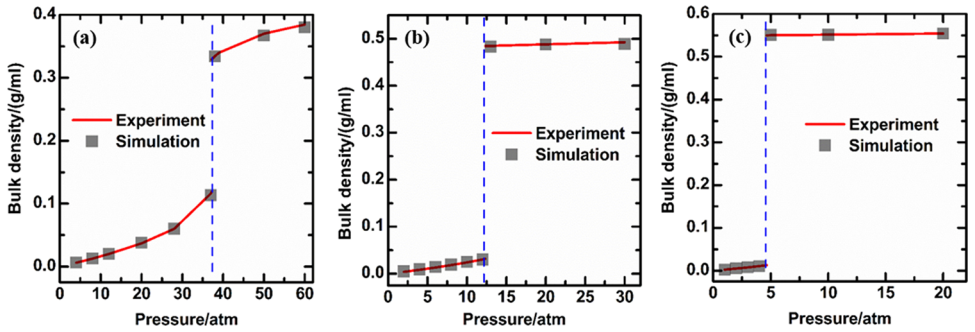

Figure 3. Bulk density vs pressure: (a) propane, (b) normal butane, and (c) normal pentane. The blue dashed line denotes the phase change from gas to liquid: T = 363.15 K.

inserting He particles randomly into the kerogen matrix box and judging whether the He particles overlap with kerogen atoms. If they do, the insertion is rejected, otherwise it is accepted. The acceptance ratio is equal to Φ, and the product of Φ and V_a is the pore volume (V_p). The skeletal density of the kerogen matrix is calculated based on the Φ and the bulk density. In S_a calculation, N_2 particles are randomly inserted around the kerogen atoms. If the N_2 particles overlap with any neighboring kerogen atoms, the insertion is rejected, otherwise it is accepted. The acceptance ratio multiplied by the total surface area of the kerogen atoms gives S_a. The calculation of PSD follows a similar procedure to that of Φ calculation. The difference lies in the size of the inserted particles increasing from zero. The porosity Φ and the pore volume V_p will decrease with the increasing size of the inserted particles. Differentiation of V_p with respect to the inserted particle size provides the PSD.

2.5. Reversibility of Kerogen Matrix and Examination of Force Field. The reversibility of the kerogen matrix is examined in terms of box side length, bulk density, skeletal density, porosity, and pore surface area versus pressure. We verify that the GCMC with PCFF+ can accurately describe the density of hydrocarbons in gas and liquid states and the saturation pressure.

The reversibility of the kerogen structural characteristics is examined in the pressure range of 1−60 atm in which the sorption and swelling will be studied. The pressure imposed on the kerogen matrix first increases from 1 to 60 atm and then decreases from 60 to 1 atm. The simulation at each pressure lasts 10 ns; the structural characteristics of the corresponding kerogen matrix are summarized in Table S1. The skeletal density (1.13 g/cm^3) is consistent with the results in the literature,[16,91] which is not affected by pressure. The bulk density increases slightly (from 0.98 to 1.00 g/cm^3) when the pressure increases from 1 to 60 atm. The box side length, the porosity, and the pore surface area decrease with increasing pressure. When pressure decreases, the structural characteristics of the kerogen matrix fully recover, providing evidence of the kerogen matrix reversibility with pressure change.

In order to examine the force field description of C_3H_8, n-C_4H_{10}, and n-C_5H_{12} and the simulation parameter settings, we perform the GCMC simulations at a temperature of 363.15 K to calculate the bulk density of each hydrocarbon at different pressures in gas and liquid states. One thousand GCMC steps are run at each pressure. Other settings of the GCMC simulations are kept the same as those in Section 2.3. Comparisons between GCMC results and experimental data[109] are made in Figure 3. As pressure increases, there is a jump in bulk density for each hydrocarbon at phase change. The saturation pressure[109] of three hydrocarbons at 363.15 K are listed in Table S2. The agreement between simulations and experiments validates the force field and GCMC parameter settings.

3. RESULTS AND DISCUSSIONS

3.1. Kerogen Matrix Swelling from Sorption. Saturation pressures of the three hydrocarbons vary significantly at 363.15 K. We investigate kerogen swelling induced by sorption of the three hydrocarbons in gas and liquid states at various pressures. The pressure ranges of our simulations for C_3H_8, n-C_4H_{10}, and n-C_5H_{12} are 1−60, 1−30, and 1−20 atm, respectively. The temperature of all simulations is kept at 363.15 K. Figure 4a shows the total uptake of the hydrocarbon

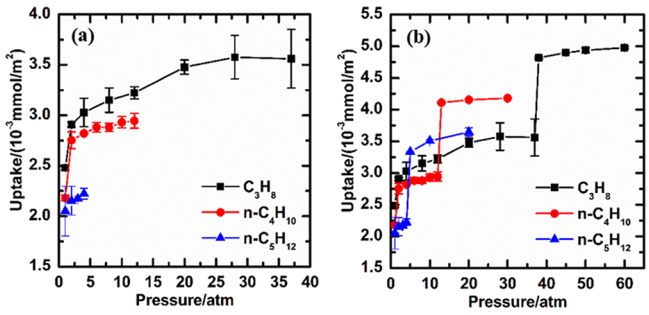

Figure 4. Total uptake of hydrocarbons vs pressure in (a) gas and (b) gas and liquid states in the flexible kerogen matrix: T = 363.15 K.

gases in the kerogen matrix. The uptake increases with pressure. The maximum uptake of C_3H_8, n-C_4H_{10} and n-C_5H_{12} gases are 3.56 × 10^{-3} mmol/m^2 at 37 atm, 2.95 × 10^{-3} mmol/m^2 at 12 atm, and 2.22 × 10^{-3} mmol/m^2 at 4 atm, respectively. The maximum hydrocarbon gas uptake decreases with increasing molecular size. The total uptake at the same pressure also decreases with molecular size. For example, at 4 atm, the uptake of C_3H_8, n-C_4H_{10}, and n-C_5H_{12} gases is 3.03 × 10^{-3} mmol/m^2, 2.82 × 10^{-3} mmol/m^2, and 2.22 × 10^{-3} mmol/m^2, respectively. The trends of gas uptake are consistent with those in our recent work.[16] Figure 4b shows the uptake of the hydrocarbons in gas and liquid states. When the pressure exceeds the saturation pressure, there is an uptake jump. The uptake of hydrocarbon liquids (4.82 × 10^{-3} mmol/m^2 at 38 atm in liquid C_3H_8, 4.11 × 10^{-3} mmol/m^2 at 13 atm in liquid n-C_4H_{10}, and 3.33 × 10^{-3} mmol/m^2 at 5 atm in liquid n-C_5H_{12}) in the kerogen matrix is much higher than that of hydrocarbon gases. For hydrocarbon liquids, increasing

https://doi.org/10.1021/acs.jpcc.0c10362
J. Phys. Chem. C 2021, 125, 8137−8147

molecular size lowers the uptake, which is the trend seen in hydrocarbon gases.

The kerogen matrix swells from hydrocarbon sorption. As Figure 5a shows, the kerogen matrix swells the most by C_3H_8

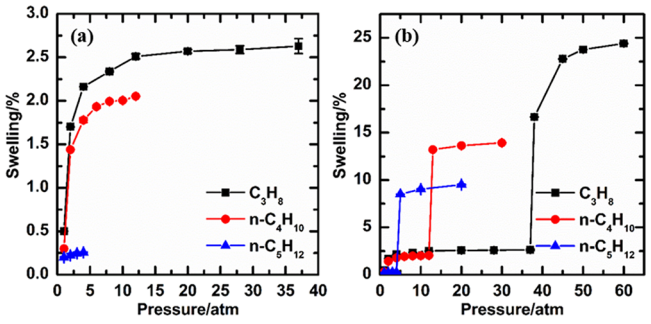

Figure 5. Swelling vs pressure of the flexible kerogen matrix in (a) gas and (b) gas and liquid states of the three hydrocarbons: T = 363.15 K

gas sorption with a maximum swelling of about 2.6% at 37 atm. The second is n-C_4H_{10} gas in which the kerogen matrix has a maximum swelling of about 2.1% at 12 atm. The swelling increases with pressure for the C_3H_8 and n-C_4H_{10} gases. The swelling by n-C_5H_{12} gas is the lowest, which is about 0.25% and has no obvious change with pressure. The kerogen matrix swells more in smaller hydrocarbon gases. This is consistent with the simulation results in ref 16. In Figure 5b, swelling of the kerogen matrix in C_3H_8, n-C_4H_{10}, and n-C_5H_{12} liquids jumps to about 16.7, 13.2, and 8.5%, respectively. There is no pronounced change with pressure in n-C_4H_{10} and n-C_5H_{12} liquids. The swelling in liquid C_3H_8 first increases with pressure then stays nearly constant. The swelling of the kerogen matrix decreases with the size increase of liquid hydrocarbon molecules, which is consistent with experiments.[41] Figures 4b and 5b provide strong evidence that Schroeder's experimental observation holds true in the kerogen–hydrocarbon system.

3.2. Displacement Fields of the Kerogen Matrix from Sorption. Figures S5–S7 present one nailed carbon atom and the displacement of a free carbon atom in the same kerogen molecule. Figure S5a–c shows front views of the kerogen matrix before and after sorption of C_3H_8 at 37.0 and 38.0 atm, respectively. The initial kerogen matrix has a side length of 48.16 Å. After exposure to C_3H_8 gas at 37.0 atm and C_3H_8 liquid at 38.0 atm, the kerogen matrix side length increases to 48.58 and 50.70 Å, respectively. The kerogen matrix swells by 2.6% at 37.0 atm and 16.7% at 38.0 atm. The swelling jump from gas to liquid is shown in Figure 5b. One kerogen molecule in the kerogen matrix is highlighted in Figure S5a–c. The nailed carbon atom and the tracked free carbon atom in the same kerogen molecule are marked as black and cyan spheres, respectively. Figure S5d–f is the magnified views of the nailed atom in the highlighted polyaromatic cluster of the kerogen matrix in Figure S5a–c. The nailed carbon atom is frozen at (69.6 Å, 65.9 Å, 78.5 Å). Figure S5g–i shows the magnified view of the tracked free atom in the hexatomic ring of the kerogen matrix in Figure S5a–c. The initial coordinate of the tracked free atom is (60.9 Å, 93.8 Å, 90.2 Å). From C_3H_8 sorption the tracked free atom moves to (62.2 Å, 92.0 Å, 89.4 Å) and (60.4 Å, 94.6 Å, 92.9 Å) at 37.0 and 38.0 atm, respectively. Similarly, Figures S6 and S7 provide a clear picture of movement of the free carbon atom from sorption of the other two hydrocarbons, i.e., n-C_4H_{10} and n-C_5H_{12} molecules, in the kerogen matrix.

In Figures S8–S10, we present full displacement fields of atoms in the kerogen molecules and magnified views of one nailed carbon atom and one tracked free atom before and after sorption of C_3H_8, n-C_4H_{10}, and n-C_5H_{12} in gas and liquid states, respectively. Figure S8a,b show the full displacement fields of the kerogen matrix from C_3H_8 gas sorption at 37.0 atm and C_3H_8 liquid sorption at 38.0 atm, respectively. The red sticks represent the kerogen matrix before sorption; the green and blue sticks are kerogen matrices after sorption of C_3H_8 in gas and liquid states, respectively. By comparing Figure S8a and Figure S8b, we clearly observe that the kerogen matrix in C_3H_8 liquid deforms and swells more than that in C_3H_8 gas. One of the nailed carbon atom and the displacement of one tracked free atom are highlighted in Figure S8c–f. Through the displacement fields, we find the nailed atom is fixed while other atoms may move as kerogen deforms. Figures S9 and S10 provide the full displacement fields of kerogen matrix from sorption of n-C_4H_{10} and n-C_5H_{12}. The nailed atoms restrain kerogen swelling; as a consequence, macroscopic swelling may reduce with respect to a truly free swelling. The effect of nailing a single atom in a kerogen molecule in swelling may be small as Figures S8–S10 suggest. Additionally, the limited nailed atoms may not affect the swelling trend and therefore validation of Schroeder's paradox is established.

3.3. Kerogen Matrix Structural Characterization. Structural characteristics of the kerogen matrix including porosity, pore surface area, and pore size distribution are affected by sorption and swelling. Figure 6 presents the

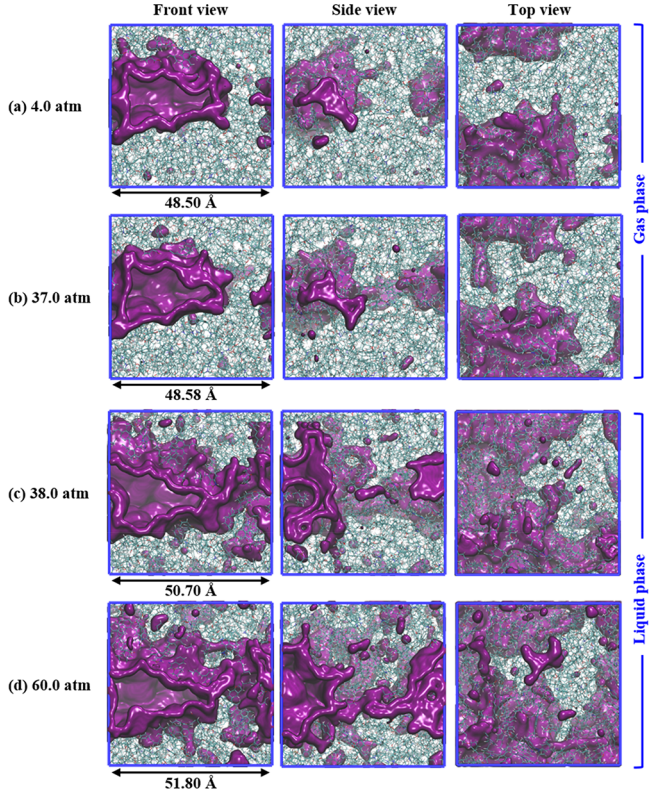

Figure 6. Front, side, and top views of the pore surface area of the flexible kerogen matrix from C_3H_8 sorption at different pressures: T = 363.15 K. The jump in size and the changes of pore surface area are pronounced from gas to liquid states.

https://doi.org/10.1021/acs.jpcc.0c10362
J. Phys. Chem. C 2021, 125, 8137–8147

kerogen matrix pore surface area at various pressures from sorption of C_3H_8. When C_3H_8 is in the gas state, most C_3H_8 molecules reside in the large pores, without changing the pore structure significantly. The sorption of C_3H_8 gas molecules expands the existing pores resulting in slight swelling of the kerogen matrix. As pressure increases and the hydrocarbon changes from gas to liquid state, new small pores are created, which are accompanied by pronounced changes in the pore surface area (Figure 6c). We interpret that some of C_3H_8 molecules dissolve in the kerogen matrix. In Figure 6c (38.0 atm) and Figure 6d (60.0 atm) where C_3H_8 is in the liquid state, in addition to the expansion of large pores, new pores and throats are created, which results in the dissolution of C_3H_8 molecules in the matrix. Pore surface areas of kerogen matrix from n-C_4H_{10} and n-C_5H_{12} sorption are, respectively, shown in Figures S11 and S12, where changes are similar to C_3H_8 sorption.

Figure 7 shows the change of the pore surface area (S_a) of the kerogen matrix with pressure from sorption of the three

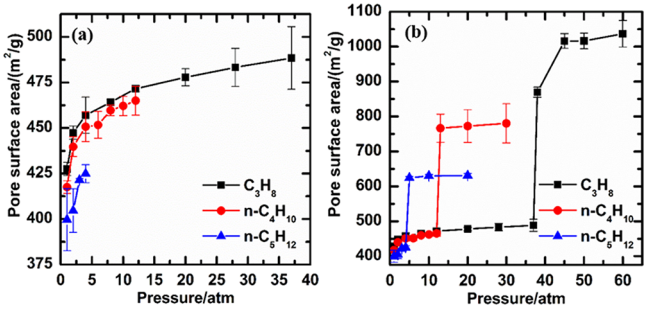

Figure 7. Pore surface area vs pressure in the flexible kerogen matrix in (a) gas and (b) gas and liquid states for the three hydrocarbons: T = 363.15 K.

hydrocarbons. The initial kerogen matrix in Figure 2c has a pore surface area of about 382 m^2/g. Figure 7a shows S_a increases from sorption in the C_3H_8, n-C_4H_{10}, and n-C_5H_{12} gases to about 488, 465, and 425 m^2/g, respectively. In Figure 7b, all three liquid hydrocarbons show a significant S_a increase. Sorption of C_3H_8, n-C_4H_{10}, and n-C_5H_{12} liquids results in high increases of the pore surface area to about 1037, 780, and 631 m^2/g, respectively. Figure 8 portrays the kerogen matrix porosity (Φ) versus pressure from sorption. The porosity of the initial kerogen matrix in Figure 2c is about 13%. Sorption of C_3H_8, n-C_4H_{10}, and n-C_5H_{12} gases increases the porosity to about 16.5, 15.9, and 14.7%, respectively. Sorption of C_3H_8, n-

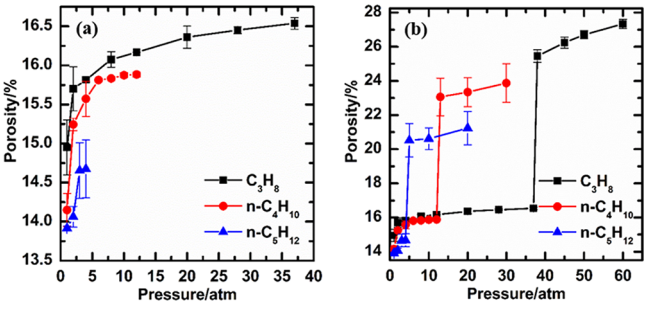

Figure 8. Porosity vs pressure in the flexible kerogen matrix in (a) gas and (b) gas and liquid states for the three hydrocarbons: T = 363.15 K.

C_4H_{10}, and n-C_5H_{12} liquids increases the porosity to about 27, 24, and 21%, respectively. Both changes of S_a and Φ from hydrocarbon sorption have similar trends to swelling changes. Smaller hydrocarbon molecules lead to a higher swelling, pore surface area, and porosity of the kerogen matrix for both hydrocarbon gases and liquids. For the same hydrocarbon, the liquid state can induce a much higher swelling, pore surface area, and porosity of the kerogen matrix than the gas state. Based on Figure 6 and Figures S11 and S12, we may conclude that hydrocarbons in the gas state lead to moderate kerogen matrix swelling from expansion of large pores; liquid hydrocarbons swell the kerogen matrix significantly not only by expanding the large pores but also by creating new pores and throats, which is accompanied with dissolution of hydrocarbons in the kerogen matrix. This results in the jump of the pore surface area (Figure 7b) and the porosity (Figure 8b). Figures S13–S15 show the distributions of the three hydrocarbon molecules in the kerogen matrix from sorption at different pressures.

The pore size distribution (PSD) of the kerogen matrix in hydrocarbon liquids and gases will provide a clear evidence of the changes in the kerogen matrix. In Figure 9, the left column portrays the PSD from sorption in hydrocarbon gases, and the right column shows the PSD from sorption in hydrocarbon gases and liquids. In C_3H_8 gas (Figure 9a) and n-C_4H_{10} gas (Figure 9c), most of the change in the PSD from sorption is

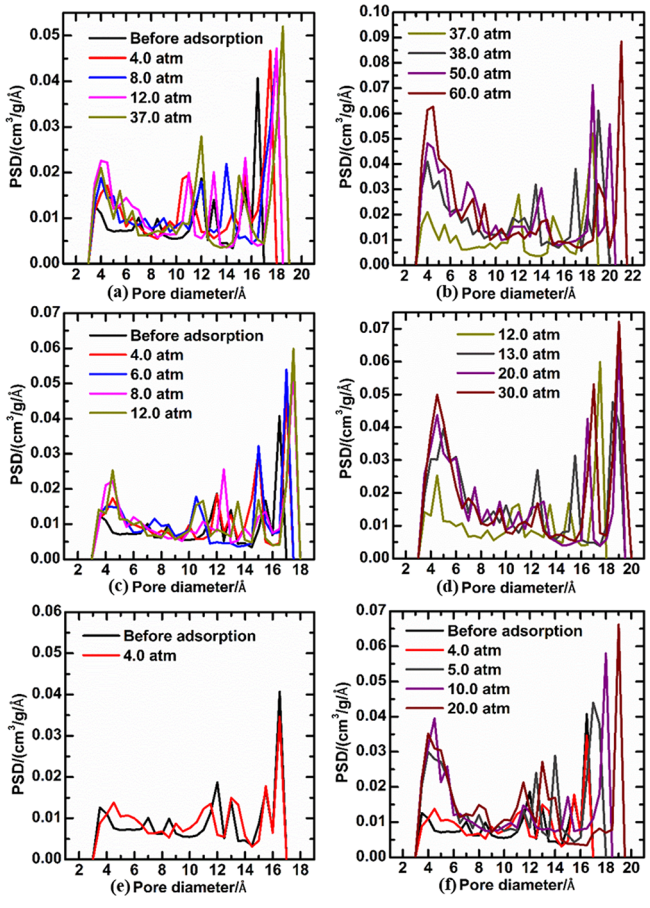

Figure 9. Pore size distribution of the flexible kerogen matrix in (a, b) propane, (c, d) normal butane, and (e, f) normal pentane. The left column shows PSD in the gas state, and the right column presents PSD in gas and liquid states.

https://doi.org/10.1021/acs.jpcc.0c10362
J. Phys. Chem. C 2021, 125, 8137–8147

from the expansion of large pores. The PSD does not change appreciably from the sorption of n-C_5H_{12} gas (Figure 9e), which is consistent with the small changes in the pore surface area (Figure 7a) and porosity (Figure 8a). In liquid hydrocarbons (Figure 9b,d,f), not only do the large pores expand but new small pores and throats are also created leading to hydrocarbon dissolution in the kerogen matrix (Figure 6c,d and Figures S11c,d and S12c,d). Figure 10a shows

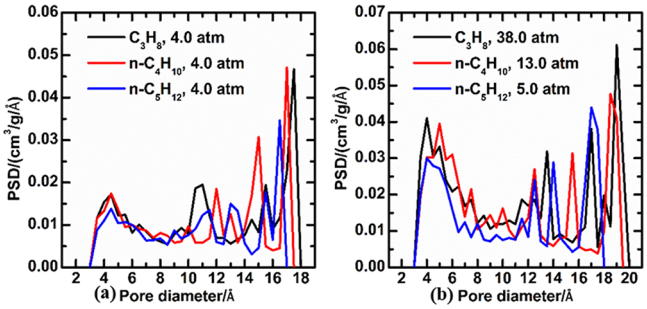

Figure 10. Pore size distribution of the flexible kerogen matrix in (a) gas and (b) liquid states for the three hydrocarbons.

changes in PSD from sorption in the three hydrocarbon gases at the same pressure. A hydrocarbon gas with a smaller molecular size can make the large pores expand more, leading to higher swelling. Figure 10b compares the PSD of kerogen matrix from sorption in different hydrocarbon liquids. In addition to making the large pores expand significantly, smaller liquid hydrocarbons also create more small pores and throats leading to a more pronounced swelling.

4. CONCLUSIONS

A flexible kerogen matrix with large pores is created through an annealing procedure in molecular dynamics simulations. A dummy particle and nailed atoms are used to create and to prevent collapse of large pores, respectively. The swelling of the created kerogen matrix induced by sorption of C_3H_8, n-C_4H_{10}, and n-C_5H_{12} in both gas and liquid states is investigated using the hybrid molecular dynamics-grand canonical Monte Carlo simulations. The changes in structural characteristics of the kerogen matrix from sorption of the three hydrocarbons are analyzed.

The main conclusions drawn from this work are as follows:

(i) Sorption of C_3H_8, n-C_4H_{10}, and n-C_5H_{12} in gas and liquid states leads to very different kerogen matrix swelling.

(ii) Smaller hydrocarbon molecules can induce higher swelling and more pronounced structural changes of the kerogen matrix in both gas and liquid states of hydrocarbons.

(iii) Sorption of hydrocarbon liquids in kerogen matrix results in much higher swelling than that of hydrocarbon gases for the same hydrocarbons at the same chemical potential. This finding is in agreement with Schroeder's experimental observation.

(iv) Sorption of hydrocarbons in both gas and liquid states results in the kerogen matrix structural deformation. The pore surface area, porosity, and pore size distribution of the kerogen matrix are altered more significantly in hydrocarbon liquids than those in hydrocarbon gases.

(v) Sorption of hydrocarbon gases mainly leads to the expansion of large pores. The large pore expansion then results in the kerogen matrix swelling. Sorption of hydrocarbon liquids leads to the expansion of large pores as well as the creation of new small pores and throats. The process allows more hydrocarbon molecules to dissolve in the kerogen matrix, thus increasing the pore surface area, the porosity, and the swelling more significantly.

We point out that capillary condensation has been neglected in our simulations. One may expect phase transition with consideration of capillary condensation and vaporization.

■ ASSOCIATED CONTENT

Supporting Information

The Supporting Information is available free of charge at https://pubs.acs.org/doi/10.1021/acs.jpcc.0c10362.

Changes of temperature and pressure versus time in the molecular dynamics relaxation procedure, pore surface area of the kerogen matrix at the end of 100-ns NPT simulation without a dummy particle, front view of the simulation box and magnified polyaromatic cluster with one marked nailed atom, a detailed discussion on the nailing of selected atoms, changes of uptake number and box side length with simulation time under 4.0 atm, structural characteristics of the kerogen matrix with 17 nailed atoms at different pressures (363.15 K), saturation pressures of C_3H_8, n-C_4H_{10}, and n-C_5H_{12} at 363.15 K, displacement fields of the kerogen matrix from sorption, front, side, and top views of pore surface area of the flexible kerogen matrix from n-C_4H_{10} and n-C_5H_{12} sorption at different pressures (363.15 K), front, side, and top views of the flexible kerogen matrix from C_3H_8, n-C_4H_{10}, and n-C_5H_{12} sorption at different pressures (363.15 K) (PDF)

■ AUTHOR INFORMATION

Corresponding Author

Abbas Firoozabadi − *Department of Chemical and Biomolecular Engineering, Rice University, Houston, Texas 77005, United States;* orcid.org/0000-0001-6102-9534; Email: firoozabadi@rice.edu

Authors

Zheng Li − *Research Center of Multiphase Flow in Porous Media, China University of Petroleum (East China), Qingdao, Shandong 266580, China; Department of Chemical and Biomolecular Engineering, Rice University, Houston, Texas 77005, United States*

Jun Yao − *Research Center of Multiphase Flow in Porous Media, China University of Petroleum (East China), Qingdao, Shandong 266580, China*

Complete contact information is available at: https://pubs.acs.org/10.1021/acs.jpcc.0c10362

Notes

The authors declare no competing financial interest.

■ ACKNOWLEDGMENTS

This work was supported by the member companies of the Reservoir Engineering Research Institute (RERI). The authors appreciate the support of the National Natural Science

Foundation of China [grant number 52034010] and the China Scholarship Council [CSC number 201906450031]. We would like to thank Dr. Tianhao Wu of RERI for helpful discussions.

REFERENCES

(1) U.S. *Energy Information Administration. Annual Energy Outlook 2020*. https://www.eia.gov/outlooks/aeo/pdf/AEO2020%20Full%20Report.pdf (accessed July 3, 2020).
(2) U.S. *Energy Information Administration. Oil and Petroleum Products Explained*. https://www.eia.gov/energyexplained/oil-and-petroleum-products/where-our-oil-comes-from.php(accessed July 3, 2020).
(3) International Energy Agency. *Oil Market Report*. https://webstore.iea.org/download/direct/2899(accessed July 3, 2020).
(4) U.S. *Energy Information Administration. Technically Recoverable Shale Oil and Shale Gas Resources: An Assessment of 137 Shale Formations in 41 Countries Outside the United States*. https://www.eia.gov/analysis/studies/worldshalegas/archive/2013/pdf/fullreport_2013.pdf(accessed July 3, 2020).
(5) Li, Z.; Yao, J.; Ren, Z.; Sun, H.; Zhang, L.; Yang, Y.; Fan, J.; Kou, J. Accumulation Behaviors of Methane in the Aqueous Environment with Organic Matters. *Fuel* **2019**, *236*, 836−842.
(6) Xie, Z.; Li, Z.; Li, J.; Kou, J.; Yao, J.; Fan, J. Electric Field-Induced Gas Dissolving in Aqueous Solutions. *J. Chem. Phys.* **2021**, *154*, No. 024705.
(7) Etminan, S. R.; Javadpour, F.; Maini, B. B.; Chen, Z. Measurement of Gas Storage Processes in Shale and of the Molecular Diffusion Coefficient in Kerogen. *Int. J. Coal Geol.* **2014**, *123*, 10−19.
(8) Martini, A. M.; Walter, L. M.; Budai, J. M.; Ku, T. C. W.; Kaiser, C. J.; Schoell, M. Genetic and Temporal Relations between Formation Waters and Biogenic Methane: Upper Devonian Antrim Shale, Michigan Basin, USA. *Geochim. Cosmochim. Acta* **1998**, *62*, 1699−1720.
(9) Jin, Z.; Firoozabadi, A. Thermodynamic Modeling of Phase Behavior in Shale Media. *SPE J.* **2016**, *21*, 190−207.
(10) Yang, Y.; Li, Z.; Cui, Z.; Sun, H.; Lu, X.; Yao, J.; Kou, J. Adsorption of Coalbed Methane in Dry and Moist Coal Nanoslits. *J. Phys. Chem. C* **2019**, *123*, 30842−30850.
(11) Perez; Devegowda, D. A Molecular Dynamics Study of Primary Production from Shale Organic Pores. *SPE J.* **2020**, DOI: 10.2118/201198-PA.
(12) Curtis, J. B. Fractured Shale-Gas Systems. *AAPG Bull.* **2002**, *86*, 1921−1938.
(13) Wang, F. P.; Reed, R. M. *Pore Networks and Fluid Flow in Gas Shales, SPE annual technical conference and exhibition*, Society of Petroleum Engineers: 2009.
(14) Ho, T. A.; Wang, Y.; Criscenti, L. J. Chemo-Mechanical Coupling in Kerogen Gas Adsorption/Desorption. *Phys. Chem. Chem. Phys.* **2018**, *20*, 12390−12395.
(15) Obliger, A.; Valdenaire, P.-L.; Capit, N.; Ulm, F. J.; Pellenq, R. J.-M.; Leyssale, J.-M. Poroelasticity of Methane-Loaded Mature and Immature Kerogen from Molecular Simulations. *Langmuir* **2018**, *34*, 13766−13780.
(16) Tesson, S.; Firoozabadi, A. Deformation and Swelling of Kerogen Matrix in Light Hydrocarbons and Carbon Dioxide. *J. Phys. Chem. C* **2019**, *123*, 29173−29183.
(17) Peng, Y.; Liu, J.; Pan, Z.; Qu, H.; Connell, L. Evolution of Shale Apparent Permeability under Variable Boundary Conditions. *Fuel* **2018**, *215*, 46−56.
(18) Zhao, H.; Lai, Z.; Firoozabadi, A. Sorption Hysteresis of Light Hydrocarbons and Carbon Dioxide in Shale and Kerogen. *Sci. Rep.* **2017**, *7*, 1−10.
(19) Ji, W.; Song, Y.; Rui, Z.; Meng, M.; Huang, H. Pore Characterization of Isolated Organic Matter from High Matured Gas Shale Reservoir. *Int. J. Coal Geol.* **2017**, *174*, 31−40.
(20) Zhao, H.; Wu, T.; Firoozabadi, A. High Pressure Sorption of Various Hydrocarbons and Carbon Dioxide in Kimmeridge Blackstone and Isolated Kerogen. *Fuel* **2018**, *224*, 412−423.
(21) Wu, T.; Zhao, H.; Tesson, S.; Firoozabadi, A. Absolute Adsorption of Light Hydrocarbons and Carbon Dioxide in Shale Rock and Isolated Kerogen. *Fuel* **2019**, *235*, 855−867.
(22) Yang, R.; Jia, A.; He, S.; Hu, Q.; Sun, M.; Dong, T.; Hou, Y.; Zhou, S. Experimental Investigation of Water Vapor Adsorption Isotherm on Gas-Producing Longmaxi Shale: Mathematical Modeling and Implication for Water Distribution in Shale Reservoirs. *Chem. Eng. J.* **2021**, *406*, 125982.
(23) Bai, J.; Kang, Y.; Chen, M.; Chen, Z.; You, L.; Li, X.; Chen, G. Impact of Surface Chemistry and Pore Structure on Water Vapor Adsorption Behavior in Gas Shale. *Chem. Eng. J.* **2020**, *402*, 126238.
(24) Chen, T.; Feng, X.-T.; Pan, Z. Experimental Study of Swelling of Organic Rich Shale in Methane. *Int. J. Coal Geol.* **2015**, *150-151*, 64−73.
(25) Heller, R.; Zoback, M. Adsorption of Methane and Carbon Dioxide on Gas Shale and Pure Mineral Samples. *J. Unconv. Oil Gas Resour.* **2014**, *8*, 14−24.
(26) Ballice, L. Solvent Swelling Studies of Göynük (Kerogen Type-I) and Beypazarı Oil Shales (Kerogen Type-Ii)☆. *Fuel* **2003**, *82*, 1317−1321.
(27) Sert, M.; Ballice, L.; Yüksel, M.; Saglam, M.; Reimert, R.; Erdem, S. Effect of Solvent Swelling on Pyrolysis of Kerogen (Type-I) Isolated from Göynük Oil Shale (Turkey). *J. Anal. Appl. Pyrolysis* **2009**, *84*, 31−38.
(28) Ballice, L.; Larsen, J. W. Changes in the Cross-Link Density of Goynuk Oil Shale (Turkey) on Pyrolysis☆. *Fuel* **2003**, *82*, 1305−1310.
(29) Hruljova, J.; Savest, N.; Oja, V.; Suuberg, E. M. Kukersite Oil Shale Kerogen Solvent Swelling in Binary Mixtures. *Fuel* **2013**, *105*, 77−82.
(30) Hruljova, J.; Järvik, O.; Oja, V. Application of Differential Scanning Calorimetry to Study Solvent Swelling of Kukersite Oil Shale Macromolecular Organic Matter: A Comparison with the Fine-Grained Sample Volumetric Swelling Method. *Energy Fuels* **2014**, *28*, 840−847.
(31) Hruljova, J.; Oja, V. Application of Dsc to Study the Promoting Effect of a Small Amount of High Donor Number Solvent on the Solvent Swelling of Kerogen with Non-Covalent Cross-Links in Non-Polar Solvents. *Fuel* **2015**, *147*, 230−235.
(32) Ayar, N.; Bilgin, B.; Atun, G. Kinetics and Equilibrium Studies of the Herbicide 2, 4-Dichlorophenoxyacetic Acid Adsorption on Bituminous Shale. *Chem. Eng. J.* **2008**, *138*, 239−248.
(33) Larsen, J. W.; Li, S. Solvent Swelling Studies of Green River Kerogen. *Energy Fuels* **1994**, *8*, 932−936.
(34) Larsen, J. W.; Li, S. Changes in the Macromolecular Structure of a Type I Kerogen During Maturation. *Energy Fuels* **1997**, *11*, 897−901.
(35) Larsen, J. W.; Li, S. An Initial Comparison of the Interactions of Type I and Iii Kerogens with Organic Liquids. *Org. Geochem.* **1997**, *26*, 305−309.
(36) Larsen, J. W.; Parikh, H.; Michels, R. Changes in the Cross-Link Density of Paris Basin Toarcian Kerogen During Maturation. *Org. Geochem.* **2002**, *33*, 1143−1152.
(37) Ertas, D.; Kelemen, S. R.; Halsey, T. C. Petroleum Expulsion Part 1. Theory of Kerogen Swelling in Multicomponent Solvents. *Energy Fuels* **2006**, *20*, 295−300.
(38) Kelemen, S. R.; Walters, C. C.; Ertas, D.; Kwiatek, L. M.; Curry, D. J. Petroleum Expulsion Part 2. Organic Matter Type and Maturity Effects on Kerogen Swelling by Solvents and Thermodynamic Parameters for Kerogen from Regular Solution Theory. *Energy Fuels* **2006**, *20*, 301−308.
(39) Savest, N.; Oja, V.; Kaevand, T.; Lille, Ü. Interaction of Estonian Kukersite with Organic Solvents: A Volumetric Swelling and Molecular Simulation Study. *Fuel* **2007**, *86*, 17−21.
(40) Savest, N.; Hruljova, J.; Oja, V. Characterization of Thermally Pretreated Kukersite Oil Shale Using the Solvent-Swelling Technique. *Energy Fuels* **2009**, *23*, 5972−5977.

https://doi.org/10.1021/acs.jpcc.0c10362
J. Phys. Chem. C 2021, 125, 8137−8147

(41) Huang, L.; Khoshnood, A.; Firoozabadi, A. Swelling of Kimmeridge Kerogen by Normal-Alkanes, Naphthenes and Aromatics. *Fuel* **2020**, *267*, 117155.
(42) Sui, H.; Yao, J. Effect of Surface Chemistry for Ch4/Co2 Adsorption in Kerogen: A Molecular Simulation Study. *J. Nat. Gas. Sci. Eng.* **2016**, *31*, 738−746.
(43) Wang, T.; Tian, S.; Li, G.; Sheng, M.; Ren, W.; Liu, Q.; Zhang, S. Molecular Simulation of Co2/Ch4 Competitive Adsorption on Shale Kerogen for Co2 Sequestration and Enhanced Gas Recovery. *J. Phys. Chem. C* **2018**, *122*, 17009−17018.
(44) Huang, L.; Ning, Z.; Wang, Q.; Qi, R.; Cheng, Z.; Wu, X.; Zhang, W.; Qin, H. Molecular Insights into Kerogen Deformation Induced by Co2/Ch4 Sorption: Effect of Maturity and Moisture. *Energy Fuels* **2019**, *33*, 4792−4805.
(45) Pathak, M.; Kweon, H.; Deo, M.; Huang, H. Kerogen Swelling and Confinement: Its Implication on Fluid Thermodynamic Properties in Shales. *Sci. Rep.* **2017**, *7*, 1−14.
(46) Pathak, M.; Huang, H.; Meakin, P.; Deo, M. Molecular Investigation of the Interactions of Carbon Dioxide and Methane with Kerogen: Application in Enhanced Shale Gas Recovery. *J. Nat. Gas. Sci. Eng.* **2018**, *51*, 1−8.
(47) Brochard, L.; Vandamme, M.; Pellenq, R. J.-M. Poromechanics of Microporous Media. *J. Mech. Phys. Solids* **2012**, *60*, 606−622.
(48) Brochard, L.; Vandamme, M.; Pellenq, R. J.-M.; Fen-Chong, T. Adsorption-Induced Deformation of Microporous Materials: Coal Swelling Induced by Co2−Ch4 Competitive Adsorption. *Langmuir* **2012**, *28*, 2659−2670.
(49) Liu, J.; Xi, S.; Chapman, W. G. Competitive Sorption of Co2 with Gas Mixtures in Nanoporous Shale for Enhanced Gas Recovery from Density Functional Theory. *Langmuir* **2019**, *35*, 8144−8158.
(50) Liu, J.; Chapman, W. G. Thermodynamic Modeling of the Equilibrium Partitioning of Hydrocarbons in Nanoporous Kerogen Particles. *Energy Fuels* **2019**, *33*, 891−904.
(51) Fuchs, A. H.; Cheetham, A. K. Adsorption of Guest Molecules in Zeolitic Materials: Computational Aspects. *J. Phys. Chem. B* **2001**, *105*, 7375−7383.
(52) Smit, B. Simulating the Adsorption Isotherms of Methane, Ethane, and Propane in the Zeolite Silicalite. *J. Phys. Chem.* **1995**, *99*, 5597−5603.
(53) Smit, B. Grand Canonical Monte Carlo Simulations of Chain Molecules: Adsorption Isotherms of Alkanes in Zeolites. *Mol. Phys.* **1995**, *85*, 153−172.
(54) Snurr, R. Q.; Bell, A. T.; Theodorou, D. N. Prediction of Adsorption of Aromatic Hydrocarbons in Silicalite from Grand Canonical Monte Carlo Simulations with Biased Insertions. *J. Phys. Chem.* **1993**, *97*, 13742−13752.
(55) Rosenbluth, M. N.; Rosenbluth, A. W. Monte Carlo Calculation of the Average Extension of Molecular Chains. *J. Chem. Phys.* **1955**, *23*, 356−359.
(56) Deroche, I.; Rives, S.; Trung, T.; Yang, Q.; Ghoufi, A.; Ramsahye, N. A.; Trens, P.; Fajula, F.; Devic, T.; Serre, C. Exploration of the Long-Chain N-Alkanes Adsorption and Diffusion in the Mof-Type Mil-47 (V) Material by Combining Experimental and Molecular Simulation Tools. *J. Phys. Chem. C* **2011**, *115*, 13868−13876.
(57) Ramsahye, N. A.; Trung, T. K.; Bourrelly, S.; Yang, Q.; Devic, T.; Maurin, G.; Horcajada, P.; Llewellyn, P. L.; Yot, P.; Serre, C. Influence of the Organic Ligand Functionalization on the Breathing of the Porous Iron Terephthalate Metal Organic Framework Type Material Upon Hydrocarbon Adsorption. *J. Phys. Chem. C* **2011**, *115*, 18683−18695.
(58) Ramsahye, N. A.; Gao, J.; Jobic, H.; Llewellyn, P. L.; Yang, Q.; Wiersum, A. D.; Koza, M. M.; Guiller, V.; Serre, C.; Zhong, C. Adsorption and Diffusion of Light Hydrocarbons in Uio-66 (Zr): A Combination of Experimental and Modeling Tools. *J. Phys. Chem. C* **2014**, *118*, 27470−27482.
(59) Cuadrado-Collados, C.; Rojas-Mayorga, C. K.; Saavedra, B.; Martinez-Escandell, M.; Osiński, J. M.; Moghadam, P. Z.; Fairen-Jimenez, D.; Silvestre-Albero, J. Reverse Hierarchy of Alkane Adsorption in Metal−Organic Frameworks (Mofs) Revealed by Immersion Calorimetry. *J. Phys. Chem. C* **2019**, *123*, 11699−11706.
(60) Rosenbach, N., Jr.; Ghoufi, A.; Déroche, I.; Llewellyn, P. L.; Devic, T.; Bourrelly, S.; Serre, C.; Férey, G.; Maurin, G. Adsorption of Light Hydrocarbons in the Flexible Mil-53 (Cr) and Rigid Mil-47 (V) Metal−Organic Frameworks: A Combination of Molecular Simulations and Microcalorimetry/Gravimetry Measurements. *Phys. Chem. Chem. Phys.* **2010**, *12*, 6428−6437.
(61) Chen, Y.; Qiao, Z.; Wu, H.; Lv, D.; Shi, R.; Xia, Q.; Zhou, J.; Li, Z. An Ethane-Trapping Mof Pcn-250 for Highly Selective Adsorption of Ethane over Ethylene. *Chem. Eng. Sci.* **2018**, *175*, 110−117.
(62) Chen, Y.; Qiao, Z.; Lv, D.; Wu, H.; Shi, R.; Xia, Q.; Wang, H.; Zhou, J.; Li, Z. Selective Adsorption of Light Alkanes on a Highly Robust Indium Based Metal−Organic Framework. *Ind. Eng. Chem. Res.* **2017**, *56*, 4488−4495.
(63) Kim, S.-I.; Lee, S.; Chung, Y. G.; Bae, Y.-S. The Origin of P-Xylene Selectivity in a Dabco Pillar-Layered Metal−Organic Framework: A Combined Experimental and Computational Investigation. *ACS Appl. Mater. Inter.* **2019**, *11*, 31227−31236.
(64) Mukherjee, S.; Desai, A. V.; Ghosh, S. K. Potential of Metal−Organic Frameworks for Adsorptive Separation of Industrially and Environmentally Relevant Liquid Mixtures. *Coord. Chem. Rev.* **2018**, *367*, 82−126.
(65) Huang, B.; Bai, P.; Neurock, M.; Davis, R. J. Conversion of N-Hexane and N-Dodecane over H-Zsm-5, H-y and Al-Mcm-41 at Supercritical Conditions. *Appl. Catal., A* **2017**, *546*, 149−158.
(66) Chempath, S.; Denayer, J. F. M.; De Meyer, K. M. A.; Baron, G. V.; Snurr, R. Q. Adsorption of Liquid-Phase Alkane Mixtures in Silicalite: Simulations and Experiment. *Langmuir* **2004**, *20*, 150−156.
(67) Macedonia, M. D.; Moore, D. D.; Maginn, E. J.; Olken, M. M. Adsorption Studies of Methane, Ethane, and Argon in the Zeolite Mordenite: Molecular Simulations and Experiments. *Langmuir* **2000**, *16*, 3823−3834.
(68) Granato, M. A.; Vlugt, T. J. H.; Rodrigues, A. E. Molecular Simulation of Propane− Propylene Binary Adsorption Equilibrium in Zeolite 4a. *Ind. Eng. Chem. Res.* **2007**, *46*, 321−328.
(69) Smit, B.; Maesen, T. L. M. Commensurate 'Freezing' of Alkanes in the Channels of a Zeolite. *Nature* **1995**, *374*, 42−44.
(70) Bai, P.; Jeon, M. Y.; Ren, L.; Knight, C.; Deem, M. W.; Tsapatsis, M.; Siepmann, J. I. Discovery of Optimal Zeolites for Challenging Separations and Chemical Transformations Using Predictive Materials Modeling. *Nat. Commun.* **2015**, *6*, 1−9.
(71) Porcheron, F.; Rousseau, B.; Schoen, M.; Fuchs, A. H. Structure and Solvation Forces in Confined Alkane Films. *Phys. Chem. Chem. Phys.* **2001**, *3*, 1155−1159.
(72) da Costa, J. M. C. P.; Cracknell, R. F.; Seaton, N. A.; Sarkisov, L. Towards Predictive Molecular Simulations of Normal and Branched Alkane Adsorption in Carbonaceous Engine Deposits. *Carbon* **2011**, *49*, 445−456.
(73) Harrison, A.; Cracknell, R. F.; Krueger-Venus, J.; Sarkisov, L. Branched Versus Linear Alkane Adsorption in Carbonaceous Slit Pores. *Adsorption* **2014**, *20*, 427−437.
(74) Dubbeldam, D.; Torres-Knoop, A.; Walton, K. S. On the Inner Workings of Monte Carlo Codes. *Mol. Simul.* **2013**, *39*, 1253−1292.
(75) Flory, P. J. *Principles of Polymer Chemistry*; Cornell University Press, 1953.
(76) Maurer, G.; Prausnitz, J. M. Thermodynamics of Phase Equilibrium for Systems Containing Gels. *Fluid Phase Equilib.* **1996**, *115*, 113−133.
(77) von Schroeder, P. L. *Ueber Erstarrungs-Und Quellungserscheinungen Von Gelatine*; W., Engelmann 1903.
(78) Vallieres, C.; Winkelmann, D.; Roizard, D.; Favre, E.; Scharfer, P.; Kind, M. On Schroeder's Paradox. *J. Membr. Sci.* **2006**, *278*, 357−364.
(79) Davankov, V. A.; Pastukhov, A. V. Paradoxes of Thermodynamics of Swelling Equilibria of Polymers in Liquids and Vapors. *J. Phys. Chem. B* **2011**, *115*, 15188−15195.

https://doi.org/10.1021/acs.jpcc.0c10362
J. Phys. Chem. C 2021, 125, 8137−8147

(80) Davankov, V. A.; Pastukhov, A. V. Swelling of Crosslinked Polymers in Liquids and Vapors. Rational Explanation of Thermodynamic Paradoxes. *Z. Phys. Chem.* **2014**, *228*, 691−710.
(81) Duan, Q.; Ge, S.; Wang, C.-Y. Water Uptake, Ionic Conductivity and Swelling Properties of Anion-Exchange Membrane. *J. Power Sources* **2013**, *243*, 773−778.
(82) Kusoglu, A.; Modestino, M. A.; Hexemer, A.; Segalman, R. A.; Weber, A. Z. Subsecond Morphological Changes in Nafion During Water Uptake Detected by Small-Angle X-Ray Scattering. *ACS Macro Lett.* **2012**, *1*, 33−36.
(83) Hussey, D. S.; Spernjak, D.; Weber, A. Z.; Mukundan, R.; Fairweather, J.; Brosha, E. L.; Davey, J.; Spendelow, J. S.; Jacobson, D. L.; Borup, R. L. Accurate Measurement of the through-Plane Water Content of Proton-Exchange Membranes Using Neutron Radiography. *J. Appl. Phys.* **2012**, *112*, 104906.
(84) Jeck, S.; Scharfer, P.; Kind, M. Absence of Schroeder's Paradox: Experimental Evidence for Water-Swollen Nafion® Membranes. *J. Membr. Sci.* **2011**, *373*, 74−79.
(85) Beers, K. M.; Yakovlev, S.; Jackson, A.; Wang, X.; Hexemer, A.; Downing, K. H.; Balsara, N. P. Absence of Schroeder's Paradox in a Nanostructured Block Copolymer Electrolyte Membrane. *J. Phys. Chem. B* **2014**, *118*, 6785−6791.
(86) Karimi, A.; Kalfati, M. S.; Rowshanzamir, S. Investigation, Modeling, and Optimization of Parameters Affecting Sulfonated Polyether Ether Ketone Membrane-Electrode Assembly. *Int. J. Hydrogen Energy* **2019**, *44*, 1096−1109.
(87) Raso, M. A.; Leo, T. J.; González-Espasandín, O.; Navarro, E. New Expressions to Determine the Water Diffusion Coefficient in the Membrane of Pem Fuel Cells. *Int. J. Hydrogen Energy* **2016**, *41*, 19766−19770.
(88) Hu, J.; Li, J.; Xu, L.; Huang, F.; Ouyang, M. Analytical Calculation and Evaluation of Water Transport through a Proton Exchange Membrane Fuel Cell Based on a One-Dimensional Model. *Energy* **2016**, *111*, 869−883.
(89) Chaudhary, S.; Sachan, V. K.; Bhattacharya, P. K. Two Dimensional Modelling of Water Uptake in Proton Exchange Membrane Fuel Cell. *Int. J. Hydrogen Energy* **2014**, *39*, 17802−17818.
(90) Tesson, S.; Firoozabadi, A. Methane Adsorption and Self-Diffusion in Shale Kerogen and Slit Nanopores by Molecular Simulations. *J. Phys. Chem. C* **2018**, *122*, 23528−23542.
(91) Ungerer, P.; Collell, J.; Yiannourakou, M. Molecular Modeling of the Volumetric and Thermodynamic Properties of Kerogen: Influence of Organic Type and Maturity. *Energy Fuels* **2015**, *29*, 91−105.
(92) Kelemen, S. R.; Afeworki, M.; Gorbaty, M. L.; Sansone, M.; Kwiatek, P. J.; Walters, C. C.; Freund, H.; Siskin, M.; Bence, A.; Curry, D. Direct Characterization of Kerogen by X-Ray and Solid-State 13c Nuclear Magnetic Resonance Methods. *Energy Fuels* **2007**, *21*, 1548−1561.
(93) Plimpton, S. Fast Parallel Algorithms for Short-Range Molecular Dynamics. *J. Comput. Phys.* **1995**, *117*, 1−19.
(94) Yiannourakou, M.; Ungerer, P.; Leblanc, B.; Rozanska, X.; Saxe, P.; Vidal-Gilbert, S.; Gouth, F.; Montel, F. Molecular Simulation of Adsorption in Microporous Materials. *Oil Gas Sci. Technol.* **2013**, *68*, 977−994.
(95) Collell, J.; Ungerer, P.; Galliero, G.; Yiannourakou, M.; Montel, F.; Pujol, M. Molecular Simulation of Bulk Organic Matter in Type Ii Shales in the Middle of the Oil Formation Window. *Energy Fuels* **2014**, *28*, 7457−7466.
(96) *Materials Design Inc. Medea® Software*. https://www.materialsdesign.com/medea-software(accessed August 2, 2020).
(97) Hockney, R. W.; Eastwood, J. W. *Computer Simulation Using Particles*; crc Press, 1988.
(98) Beckers, J. V. L.; Lowe, C. P.; De Leeuw, S. W. An Iterative Pppm Method for Simulating Coulombic Systems on Distributed Memory Parallel Computers. *Mol. Simul.* **1998**, *20*, 369−383.
(99) Waldman, M.; Hagler, A. T. New Combining Rules for Rare Gas Van Der Waals Parameters. *J. Comput. Chem.* **1993**, *14*, 1077−1084.
(100) Nosé, S. A Unified Formulation of the Constant Temperature Molecular Dynamics Methods. *J. Chem. Phys.* **1984**, *81*, 511−519.
(101) Nosé, S. A Molecular Dynamics Method for Simulations in the Canonical Ensemble. *Mol. Phys.* **1984**, *52*, 255−268.
(102) Nosé, S.; Klein, M. L. A Study of Solid and Liquid Carbon Tetrafluoride Using the Constant Pressure Molecular Dynamics Technique. *J. Chem. Phys.* **1983**, *78*, 6928−6939.
(103) Hoover, W. G. Constant-Pressure Equations of Motion. *Phys. Rev. A* **1986**, *34*, 2499.
(104) Wu, T.; Firoozabadi, A. Effect of Microstructural Flexibility on Methane Flow in Kerogen Matrix by Molecular Dynamics Simulations. *J. Phys. Chem. C* **2019**, *123*, 10874−10880.
(105) Koretsky, M. D. *Engineering and Chemical Thermodynamics*; John Wiley & Sons, 2012.
(106) Barnes, C. S. *Thermosolver: An Integrated Educational Thermodynamics Software Program*. Oregon State University, 2006.
(107) Gelb, L. D.; Gubbins, K. E. Characterization of Porous Glasses: Simulation Models, Adsorption Isotherms, and the Brunauer− Emmett− Teller Analysis Method. *Langmuir* **1998**, *14*, 2097−2111.
(108) Gelb, L. D.; Gubbins, K. E. Pore Size Distributions in Porous Glasses: A Computer Simulation Study. *Langmuir* **1999**, *15*, 305−308.
(109) National Institute of Standards and Technology. *Thermophysical Properties of Fluid Systems*. https://webbook.nist.gov/chemistry/fluid/(accessed August 2, 2020).

https://doi.org/10.1021/acs.jpcc.0c10362
J. Phys. Chem. C 2021, 125, 8137−8147